Arsenic speciation in the dispersible colloidal fraction of soils from a mine-impacted creek

Susana Serrano[a], Miguel Angel Gómez-González[b] , Peggy A. O'Day[c], Francisco Laborda[d], Eduardo Bolea[d], and Fernando Garrido[b]

[a]Institute of Agrochemistry and Food Technology, CSIC, Agustín Escardino 7, 46980 Paterna Valencia, Spain

[b]National Museum of Natural Sciences, CSIC, José Gutiérrez Abascal 2, 28006 Madrid, Spain

[c]School of Natural Sciences, University of California, Merced, CA 95343, USA

[d]Group of Analytical Spectroscopy and Sensors (GEAS), Institute of Environmental Sciences (IUCA), University of Zaragoza, Pedro Cerbuna 12, 50009 Zaragoza, Spain

* Corresponding author (fernando.garrido@mncn.csic.es); Tel.: +34 917452500; Fax: +34 915640800

1

ABSTRACT

Arsenic and iron speciation in the dispersible colloid fraction (DCF; 10-1000 nm) from an As-rich mine waste pile, sediments of a streambed that collects runoff from waste pile, the streambed subsoil, and the sediments of a downstream pond, was investigated by combining asymmetrical-flow field-flow fractionation (AsFlFFF)/inductively-coupled plasma-mass spectrometry (ICP-MS), transmission electron microscopy (TEM) and X-ray absorption (XAS) spectroscopy. Calcium, Fe and As (Fe/As molar ratio~1) were the main components of the DCF from waste pile. TEM/EDS and As and Fe XAS analysis revealed the presence of nanoparticle scorodite in this same DCF, as well as Fe nanoparticles in all samples downstream of the waste pile. Arsenic and Fe XAS showed As(V) adsorbed onto nanoparticulate ferrihydrite in the DCF of downstream samples. Micro-X-ray fluorescence indicated a strong correlation between Fe and As in phyllosilicate/Fe^{3+} (oxi)hydroxide aggregates from the sediment pond. Fractionation analysis showed the mean particle size of the DCF from the streambed sample to be smaller than that of the streambed subsoil and sediment ponds samples. These results show that an important and variable fraction of As may be bound to dispersible colloids that can be released from contaminated soils and transported downstream in natural systems.

1. Introduction

Understanding the release of colloids from soils and sediments, and their association with contaminants, is essential when evaluating pollutant transport processes [1-7]. The *in situ* mobilization and transport of colloids in soils depends on the latters' physico-chemical characteristics (presence of organic matter, clay minerals, pH, ionic strength, etc.), and the reigning hydrodynamic conditions (flow velocity and soil saturation) [8, 9]. Once a colloid has been mobilized, its transport is controlled by its size and stability in solution, i.e., its tendency to aggregate. Aggregation is controlled mainly by the balance of attractive and repulsive forces between particles [10]. The presence in solution of ions of opposite charge to those on the surface of a colloid, and an increment in the ionic strength of the soil solution and/or any runoff, increases aggregation, while the surface coating of colloids with organic matter enhances colloid stability [11]. Colloids can strongly bind metals and other pollutants in soils and aquifers. In soils and sediments impacted by mining wastes, the mobility of As and other metals is affected by the release and transport of nanoparticles from the soils and As-colloid adsorption phenomena.

The characterization of natural colloids requires the use of fractionation and analytical techniques that minimize sample perturbation. One option is asymmetrical-flow field-flow fractionation (AsFlFFF), in which colloids are separated according to their diffusion against a flow-field perpendicular to a carrier flow [12, 13]. The AsFlFFF has been used couple to inductively-coupled plasma-mass spectrometry (ICP–MS) to determine the elemental composition of colloids and their particle size distribution [12, 14, 15]. This allows the relationship between trace metal(oids) concentrations and colloid particle size to be established. However, elemental analysis alone provides no information about the molecular-scale chemical association of metal(oids) and colloids, which

determines the potential bioavailability and health impacts of dispersed contaminants, and helps predict metal-colloid stability.

Synchrotron X-ray methods have been used to characterize natural colloids and their association with As in mine systems. Slowey et al. [16] described the transport of As(V) when adsorbed onto colloidal ferrihydrite and jarosite in columns packed with mine tailings. Zanker et al. [17] showed that mine wastes contained As within nanometer jarosite-like particles. Additionally, AsFlFFF/ICP-MS has revealed colloid-bound As in abandoned mine tailings [7], while selective sequential extraction, high resolution ICP-MS and transmission electron microscopy (TEM) [18] have revealed nanoparticles sequestered by metal-contaminated mine sediments.

In this work, the dispersible colloid fractions (DCFs) (10-1000 nm) of a mine waste pile and its adjacent sediments and soils were examined to determine their elemental and mineral composition as a function of colloid size. The As and Fe speciation was also examined, as was the partitioning of As and companion metals between the DCF and the fraction of their total amount that remained dissolved. Understanding the relationship between the composition of natural colloids, and soils and sediments properties, as well as the colloid-contaminant association, is crucial in contaminant transport studies.

2. Materials and methods

2.1. Sample collection and description

Samples were collected from an abandoned smelting factory in Guadalix de la Sierra (Madrid, Spain) where arsenopyrite encapsulated in quartz was mined and processed for wolfram extraction during the Second World War (Fig. 1). Arsenic-rich residues were dumped nearby and pose a public health problem [19]. Four types of sample were collected: (1) samples (0-10 cm depth) from the main waste pile (WP) [19] (dumped on the

soil surface); (2) sediments from the bed of a small stream originating at the WP that collects runoff (samples RB2 at 17 m from the WP and at 0-5 cm depth , and RB at 26 m from WP and at 0-10 cm depth); (3) the streambed subsoil (SS) (at 26 m from the WP and at 10-20 cm depth of), and (4), the sediment from a downstream pond (SP) (at 58 m from the WP and at a depth of 0-5 cm) that collects runoff from the stream (Fig. 1).

Characterization methods are described in the Electronic Annex (EA).

2.2. Dispersible colloid fraction: preparation and pre-fractionation

The maximum amount (mg kg^{-1} soil) of potentially releasable colloids from the different samples was termed dispersible colloid fraction (DCF). The DCF was extracted from all samples based on a protocol described elsewhere [13] with modifications (Fig. 2). Preparation and pre-fractionation methods are given in EA.

2.3. Colloid characterization

2.3.1. AsFlFFF-ICP-MS

The distribution of particle size and the concentration of associated metal(oid)s in the <1000 nm fraction was determined by AsFlFFF-ICP-MS (see Table EA-2 for operating conditions).

In AsFlFFF, a surfactant (SDS, 0.01% w/v) adjusted to pH 4.5 (close to the original pH) was used as a carrier solution for the <1000 nm fraction from the WP, RB2, RB and SS samples; for the SP sample it was adjusted to pH 6.5. The carrier was degassed by an on-line vacuum degasser prior to use. Sample loops of 20 and 100 µL were used throughout depending on the element concentrations detected [20]. Colloid sizes and calibration standards; (details in EA) were detected using a UV-vis diode array detector (Shimadzu). On-line multi-element quantification was performed using an ELAN DRC-e ICP-MS (Perkin Elmer). The samples were introduced into the ICP-MS using a glass concentric slurry nebulizer and a cyclonic spray chamber (Glass Expansion). An internal

standard solution of 50 ng mL^{-1} Rh (Merck) was pumped into the mobile phase at 0.3 ml min^{-1} for correction of instrumental drift. ICP-MS data acquisition and recovery calculation details are in Table EA-3.

2.3.2.Element concentrations

The element concentrations of the DCF of each sample were analyzed using an OPTIMA 4300DV ICP-optical emission spectrometer (ICP-OES) (Perkin-Elmer) after microwave digestion with HF+HNO$_3$+HCl followed by H$_3$BO$_3$. The DFs (<10 nm fractions) were analyzed using an ELAN DRC-e ICP-MS spectrometer (Perkin Elmer).

The total carbon concentration in the DCF was determined by combustion using a 2400 Series II CHNS/O Elemental Analyzer (Perkin Elmer). The mass retained on the ultrafiltration membranes was determined gravimetrically.

2.3.3. Transmission electron microscopy

Aliquots of the <1000 nm fraction from the WP, RB and SS were examined using a CM200FEG transmission electron microscope (TEM) (Philips,) (See EA).

2.3.4. Microfocused synchrotron X-ray fluorescence

Chemical mapping was performed on the <1000 nm SP fraction using synchrotron microfocused X-ray fluorescence (μXRF) at the Stanford Synchrotron Radiation Lightsource (SSRL) laboratory (on Beamline 2-3) (See EA).

2.3.5. Arsenic and iron X-ray absorption spectroscopy

Arsenic and Fe K-edge spectra of DCF samples, and of a reference DCF sample of As adsorbed onto ferrihydrite (termed As(V)_Fh_coll; see EA for details), were collected at the European Synchrotron Radiation Facility (ESRF; 6 GeV, 100 mA) (bending-magnet BM25A Beamline). Methods are described in EA. Spectra were analyzed using Athena software [21] for linear combination fits, and EXAFSPAK software [22] for shell-by-shell fits. Data collection and analysis are in EA.

3. Results

3.1. DCF composition and size distribution

Table 1 shows element concentrations of the DCF of the different samples. Figure 3 shows their relative molar proportions. Calcium was the major element (3.5 mol kg coll^{-1}) of the DCF of the WP sample (WP$_{DCF}$), followed by As and Fe with a Fe/As mole ratio ~ 1. Iron and Al were the major elements in RB2$_{DCF}$, RB$_{DCF}$ and SS$_{DCF}$. Carbon accounted for 39% of the element composition in SP$_{DCF}$, and Al 48% (Fig. 3). The RB$_{DCF}$ had the highest Fe concentration of all samples while the SS$_{DCF}$ had the highest Al concentration. The RB$_{DCF}$ and SP$_{DCF}$ had slightly lower (and similar) Al concentrations. The RB$_{DCF}$ had the highest Fe/Al molar ratio, followed by RB2$_{DCF}$, SP$_{DCF}$ and SS$_{DCF}$.

The As concentration fell with distance from the WP; indeed, a large difference in As concentration was seen between the WP$_{DCF}$ (0.25 mol kg coll^{-1}) and the RB2$_{DCF}$ (0.08 mol kg coll^{-1}), falling further for the RB2$_{DCF}$, RB$_{DCF}$, SS$_{DCF}$ and SP$_{DCF}$ (Fig. 1). An increase in the Fe/As molar ratio was observed from the WP to the SP positions (Table 2). Calcium represented 12% of the elemental composition of the RB2$_{DCF}$ but less than 2% of that of the RB$_{DCF}$, SS$_{DCF}$ and SP$_{DCF}$ (Fig. 3). Lead was only detected in WP$_{DCF}$; Cu and Zn were below the detection limit. The SS$_{DCF}$ showed the highest Cu concentration of the downstream samples (0.05 mol kg^{-1}) (SS$_{DCF}$ >RB$_{DCF}$ >SP$_{DCF}$), while the RB2$_{DCF}$ showed the highest Zn concentration (0.01 mol kg^{-1}) (RB2$_{DCF}$ > RB$_{DCF}$>SS$_{DCF}$> SP$_{DCF}$).

Figure 4 shows the AsFlFFF-ICP-MS fractograms for the RB, SS and SP <1000 nm fractions. Given the low colloid mass (per mass of bulk sample) of the WP$_{DCF}$ and RB2$_{DCF}$ (2634 mg kg^{-1} and 840 mg kg^{-1} respectively), and the high conductivity of the WP suspension (Table EA-1) no reliable fractograms were obtained. The <1000 nm fractions had different colloid size distributions but similar Al, Ca, Fe, As, Cu, Zn and Pb concentration distributions. The <1000 nm fraction of RB was characterized by particle

size and element concentration maxima at ~30 nm; the maximum element concentration was also associated with this particle size (Fig. 4a). The single-peak element concentration suggests particle homogeneity. For the <1000 nm fraction of the SS sample, two maxima were observed in the colloid size distribution, at 55 and 175 nm (Fig. 4b). The SP fractogram showed a wide distribution with a broad maximum between 55 and 100 nm (Fig. 4c).

3.2. TEM-EDX and μXRF

Particulate scorodite (~80 nm in diameter) was observed and identified by TEM-EDX in the WP_{DCF} (Fig. 5a). In the $RB2_{DCF}$, TEM-EDX showed particle aggregates of <50 nm and high concentrations of Si, Al and Fe, suggestive of clay minerals and Fe hydroxides (Fig. 5b). In the RB_{DCF}, 30 nm Fe nanoparticles formed chains or aggregates associated with Si, Ca, Mn and Cu (Fig. 5c, 5d). Iron nanoparticles (10 nm) forming larger aggregates (~50 nm in diameter) were observed in the SS_{DCF} (Fig. 5e). Arsenic associated with Fe particles in the SS_{DCF} was observed by EDX analysis (data not shown). The SP_{DCF} contained aggregates of small nanoparticles (~10 nm); Fe, Si, Al, Ca, Mg and As were detected by EDX, indicating these aggregates to be heterogeneous. Synchrotron μXRF maps (mapping area 1x1 μm^2) of the SP_{DCF} indicated a correlation between As and Fe in aggregated nanoparticles (150-250 nm) (Fig. 5g and h).

3.3. Arsenic and iron XAS of colloids

Normalized As XANES of three As reference spectra -natural scorodite [23], As absorbed onto ferrihydrite (As(V)_Fh; As/Fe ratio 0.012) [24], and colloid-extracted As absorbed onto ferrihydrite (<1 μm) (As(V)_Fh_coll; As/Fe ratio 0.09 [this study])- were compared with those of the DCF samples (Fig. 6). The As(V)_Fh and As(V)_Fh_coll reference spectra were similar, although their post-edge spectral features were not identical. The As K-edge XANES spectra of all DCF samples indicated that As was

8

present only as As(V) (absorption maxima 11874.5-11875.5 eV) (Fig. 6). The XANES spectra of all DCF samples, except WP$_{DCF}$, resembled that of either As(V)_Fh or As(V)_Fh_coll, with small differences associated with a post-edge absorption feature at around 11895 eV (Fig. 6). The LCF of the WP$_{DCF}$ As XANES spectrum indicated a mixture of scorodite (61%) and As(V)_Fh (39%) (Table 2). The XANES spectra of DCFs of the downstream samples were fit best using only the As(V)_Fh reference spectrum (Table 2).

Shell-by-shell quantitative analysis of the WP$_{DCF}$ As EXAFS spectrum indicated a bonding environment for As similar to that of scorodite, with similar coordination numbers and interatomic distances (Table 2, Fig. 6). Fits to RB$_{DCF}$ and SP$_{DCF}$ spectra gave an As-Fe distance of 3.31-3.32 Å, similar to that fit for the As(V)_Fh_coll reference spectrum. For comparison, the fit of As(V)_Fh_coll reference spectrum yielded an As-O first-shell distance of 1.69Å (N$_{As-O}$=4, fixed) and an As-Fe distance of 3.28 Å. This As-Fe distance was shorter than the two As-Fe distances (3.38 and 3.52 Å) obtained from the fit of the reference spectrum of As sorbed to ferrihydrite (As(V)_Fh) (Table 2).

Linear combination fits of Fe XANES spectra showed that the WP$_{DCF}$ was dominated by scorodite (83%) and an Fe(III)-oxide phase (16%) that best matched the As(V)_Fh_coll reference spectrum (Fig. 7, Table 3). The two best-fit components for the RB$_{DCF}$ and SS$_{DCF}$ were smectite (SAz-1) and As(V)_Fh_coll (Fig. 7, Table 3). The SP$_{DCF}$ spectrum was fit best with reference illite (IMT-1 Fe) (60%) and As(V)_Fh_coll (40%) spectra. The RB2$_{DCF}$ spectrum was fit with only the As(V)_Fh_coll spectrum. The reference compounds used in the XANES analysis were also used in LCF of the Fe EXAFS spectra. The EXAFS LCFs overestimated crystalline mineral fractions such as illite compared with amorphous phases such as ferrihydrite because of the stronger second-neighbor backscattering in crystalline materials [25].

3.4. Composition of dispersible colloid and dissolved fractions and bulk sample properties

The bulk WP sample had low pH (3.25), and its main minerals were scorodite, gypsum, quartz and hematite (Table EA-1; Fig. EA-1). Chemical analysis revealed the WP_{DCF} to have high As (1.8 mol kg^{-1}), Fe (3.5 mol kg^{-1}) and Ca (1.1 mol kg^{-1}) contents, (Fig. 3) although these represent only small fractions of the bulk sample contents (<0.04% for As and Fe, and 0.8% for Ca). The Fe/As molar ratio of the WP_{DCF} (Fe/As=0.94) was half that of the bulk WP (1.96). The WP_{DCF} and $RB2_{DCF}$ the smallest colloid masses per mass of bulk sample (Table 1).

The bulk RB2 sample, collected close to the waste pile (Fig. 1), had more acidic pH (3.86) and higher As and Fe concentrations than the RB, SS and SP bulk samples. However, when normalized to the mass of the bulk sample, the As and Fe concentrations of the $RB2_{DCF}$ were lower than in the other downstream samples (0.2 % and 0.07 % of the total As and Fe contents of the RB2 bulk sample). The bulk RB2 and the $RB2_{DCF}$ had the lowest Ca concentrations. Zinc and Pb concentrations of the RB2, RB, SS and SP bulk samples were similar. The RB2 bulk sample was richer in Cu than in Zn or Pb. Copper concentration increased in the downstream RB and SS bulk samples, but decreased in the SP bulk sample. A similar trend was observed in the DCF of these samples (although no Cu was detected in $RB2_{DCF}$) (Fig. 8). The bulk RB sample had a higher pH (4.3) and higher organic carbon (OC) content than the bulk RB2 sample (Table EA-1). The total As concentration of the RB2 bulk sample was one order of magnitude greater than that of the RB bulk sample. In contrast, the As concentration per mass of bulk sample in RB_{DCF} was greater than in $RB2_{DCF}$ (Fig. 8). The RB_{DCF} As concentration accounted for more than 35% of the total As in the bulk sample. The XRD pattern of the RB2 and RB bulk samples showed hematite, muscovite, quartz and feldspar to be the primary minerals (Fig. EA-1). The total element composition of the SS bulk sample was similar to that measured for the

RB bulk sample (Table EA-1), except that no OC was measured in the SS sample. The SS bulk sample had slightly higher pH (4.5) than the RB bulk sample and similar XRD pattern, although no hematite was detected (Fig. EA-1). The SS_{DCF} had greater colloid mass than the RB_{DCF}, and contained less As and Fe, but more Ca (Fig. 8). The greatest colloid mass per mass of bulk sample was obtained for the SP bulk sample (17644 mg kg^{-1}); the bulk SP (Table EA 1) and SP_{DCF} (Table 1) had the highest C contents and pH (pH= 6.2) of all. The total As concentration of the SP bulk sample (2.3 mmol kg^{-1}) was almost double that of the RB and SS bulk samples (~1.3 mmol kg^{-1}), while the Fe and Ca contents were similar in all three. In contrast, the As and Fe concentrations were lower in the SP_{DCF} than in the RB_{DCF}, and higher than in the SS_{DCF}, while the Ca concentration was lower in the SP_{DCF} than in the RB_{DCF} and SP_{DCF} (Fig. 8). The As concentration of the SS_{DCF} and SP_{DCF} were 0.12 and 0.24 mmol kg soil^{-1} respectively, representing ~10 % of the total As concentration of the corresponding bulk samples.

Low As and Fe concentrations were found in all dissolved fractions DFs(<10 nm) (Table EA-5, Fig. 8). The SS_{DF} had the highest As concentration, (0.5% of the total As content of the bulk SS sample). Iron was detected only in the WP_{DF} and $RB2_{DF}$. The Al concentration was low in all the dissolved fractions. The DF concentrations of Ca, Cu, Zn, and Pb were higher than in the corresponding DCFs (especially with respect to WP and RB2) (Fig. 8). Finally, lower Ca, Cu and Zn concentrations were observed in the RB_{DF}, SS_{DF} and SP_{DF} than in the WP_{DF} and $RB2_{DF}$

4. Discussion

4.1. DCF composition and As and Fe speciation

Nanoparticle scorodite was the main As mineral phase in the WP_{DCF}, and it has a local atomic structure similar to that of crystalline scorodite at particle sizes of ~80 nm in diameter). There was no evidence for nanoparticulate scorodite in any other DCF,

suggesting dissolution down-gradient of the WP despite its reported low solubility and high stability at pH 3-4 [26].

In the downstream samples, As was mainly associated with Fe(III) oxide phases. The EXAFS spectra showed similar As-Fe interatomic distances in the RB_{DCF} and SP_{DCF} (3.32 Å and 3.31 Å respectively), comparable to that obtained in EXAFS analysis of As(V) adsorbed onto colloidal 2-line ferrihydrite (3.28 Å), but shorter than values obtained in the EXAFS fit of As(V) adsorbed onto bulk 2-line ferrihydrite (fit two Fe shells at 3.38 Å and 3.52 Å) [27]. Differences in the local As(V) bonding environment between these two reference spectra are probably related to differences in their As/Fe molar ratios and the smaller particle size of colloidal ferrihydrite. The greater proportion of Al to Fe in the SS_{DCF} compared to RB_{DCF} and SP_{DCF} might explain the lack of strong second-neighbor backscattering in the SS_{DCF} spectrum compared to the RB_{DCF} or SP_{DCF} spectra. The Fe XANES results for the SP_{DCF} suggest a spectral contribution from an Fe-bearing illite-type phase (~60%) rather than a smectite phase in addition to iron oxide-type phases. The high Al concentration of the DCFs of the downstream samples, and the TEM-EDS observations, indicate the presence of aluminosilicates generally associated with Fe-rich particles. The adsorption capacity of Fe(III) oxides and clay minerals for Ca, Cu, Zn and Pb [28, 29] would explain their presence in the downstream sample DCFs (Fig. 4), although this interaction depends on the pH of the bulk samples (see next section). The SP_{DCF} had the greatest colloid mass of all. This might be related to its high OC content, which can increase the stability of iron-rich nanoparticles [30]. TEM and μXRF analysis of SP_{DCF} showed the formation of aggregates with strong Fe/As correlations, supporting the idea that As adsorbs onto the Fe (III) phases, as indicated by As XAS.

4.2. DCF composition and bulk sample properties

The presence of organic matter, circum-neutral pH, and low ionic strength, increase the stability of soil colloids [9, 11]. Thus, the high colloid mass associated with the SP_{DCF} (Table 1) is likely the result of the high pH, high OC content and low ionic strength of the SP bulk sample (Table EA-1). Both the SP and RB bulk samples have similar C contents; however, the higher pH of the former may promote the release of organic matter [31], explaining the higher OC of the SP_{DCF} than the RB_{DCF}. In contrast, the WP_{DCF} and $RB2_{DCF}$ showed the smallest colloid masses, probably related to the acidic pH and undetectable OC content of their bulk samples. This might also be related to the high Ca^{2+} concentration of the WP bulk sample hindering colloid release [32, 33]. The higher Ca^{2+} content of the SS_{DCF} than of the RB_{DCF} or SP_{DCF} might also be associated with the formation of the large aggregates observed (Fig. 5).

Normalized to the bulk sample mass, the higher As concentration of the RB_{DCF} (>35% of the total As in RB) compared to the SS_{DCF} and SP_{DCF} may be related to its smaller colloid size. The specific surface area is related to the particle size and determines the adsorption capacity of colloids [2]. Accordingly, higher As concentrations are expected for samples with smaller particles sizes, such as the RB bulk sample. This trend, however, was not seen for Ca, Cu, Zn or Pb, since their retention on Fe (oxy)hydroxide and clay nanoparticles at the pH of the RB (pH=4.3) is not favored.

The Fe (oxy)hydroxide nanoparticles present in the DCFs may either have formed in the DCF or have been mobilized from the bulk samples. In the SP bulk sample, the precipitation of Fe oxide particles might be associated with its higher pH [31]; Fe solubility decreases with increasing pH [34]. Given the acidic pH of the remaining samples, Fe (oxy)hydroxide and clay mineral particles would originate mostly through their mobilization from the bulk samples. Calcium, Cu, Zn and Pb partitioning between the DCF and DF of the samples might also be affected by pH. In general, samples with lower soil

13

pH (WP and RB2) had DCFs with lower cation concentration, but DF with higher dissolved cation concentration. The opposite behavior was observed in samples which had higher pH, with the exception of Cu in SP, for which higher Cu concentration was observed in the DF than in the DCF.

4.3. Implications for As and metal mobility

Arsenic was present in the DCF of all samples downstream of the WP mostly associated with colloid-size Fe-(oxy)hydroxides. In the corresponding DFs (< 10 nm), low As concentrations were observed. The relative amounts of As bound to colloids varied from 1% to 35% of the total As concentration in the bulk samples, depending on their pH, OC content, ionic strength, and the size distribution of the natural nanoparticles (which determine their surface reactivity [35]). In spite of the differences in these variables, and of differences in DCF particle sizes, As adsorption onto Fe-(oxy)hydroxides persisted in the DCF of all the downstream samples, indicating the high affinity of As for nanoparticulate Fe-(oxy)hydroxides [36] and their potential mobility. In addition to the concentration of Fe-(oxy)hydroxide nanoparticles and their potential function as As carriers, the transport of trace metals on colloidal particles depends on local water chemistry [1, 35]. Since the extraction of the DCF from the samples was performed *ex situ* using a 1:10 dried bulk sample/solution ratio, results can only be extrapolated to field conditions resulting after rain events following extended dry periods. However, they might represent the potentially removable colloid-bound and dissolved fractions of contaminant elements in natural systems. Further work should include examining the release of colloids *in situ* in seasonally variable environments.

5. Conclusions

This work showed that up to one third of the total As present in bulk samples collected from a mine site and adjacent soils and sediments, was associated with the colloid fraction and very low concentrations were measured in the dissolved fraction (<10 nm). The acidity, OC content and Ca concentration of the samples were closely related to the stability or aggregation of colloids, and thus the particle size distribution. Nanoparticle scorodite was only found in the wastepile samples, which suggest the dissolution of this mineral in downstream samples. The persistent association of As and ferrihydrite in the DCF of samples collected downstream of the WP reflects the high affinity of As for nanosize Fe-(oxy)hydroxides particles irrespective of the pH or OC content, and suggests a potential role of these nanoparticles as As carriers in natural systems. The combination of AsFIFFF-ICP-MS and X-ray absorption spectroscopy provides fundamental information on the partitioning of contaminants in colloid-size particles, as well as their speciation, that contributes to understanding metal(oid) pollution processes in natural systems.

6. Acknowledgements

performed at *Servicio General de Apoyo a la Investigación-SAI (Universidad de Zaragoza).*

Appendix A. Supplementary data

FIGURE CAPTIONS

1. Location of the area of study. A: Abandoned processing plant with waste pile in the foreground. B: Plan of sampling locations (WP, RB2, RB, SS, SP).

2. Procedure for fractionation and characterization of DCF and DF extracted from bulk samples.

3. Elemental composition (mol kg^{-1} colloid) of the DCF (10-1000 nm).

4. AsFFF-ICP-MS fractograms for the <1000 nm fractions of the RB, SS and SP samples showing ICP-MS counts per second (cps) as a function of particle size.

5. Transmission electron microscopy and energy dispersive X-ray spectroscopy analysis of colloid fractions. a) Scorodite nanoparticle in WP, b) heteroaggregates (clay minerals and iron particles) in RB2, c) and d) iron nanoparticles and aggregates in RB, e) aggregates of iron nanoparticles in SS, and f) arsenic identified in aggregates of iron nanoparticles and clay minerals in SP, g) and h) synchrotron μXRF element maps of colloid particles in SP.

6. Arsenic K-edge XANES, EXAFS and Fourier transformations (FT) of DCF from the WP, RB, SS and SP samples (only XANES was performed for RB2). The XANES spectra show the deconvolution of the LCF with the reference scorodite [23] and arsenate adsorbed onto hydrous ferric oxide [As(V)_Fh] [24] (fit results in Table 2). EXAFS were fit using a nonlinear least squares shell-by-shell approach (fitting results in Table EA-6).

7. Iron K-edge XANES, EXAFS and Fourier transformations (FT) of the DCF from the WP, RB2, RB, SS and SP samples. XANES show the deconvolution of the LCF with the reference smectite (SAz-1) (Clay Minerals Society Source Clays Repository), scorodite [23], and the reference As adsorbed onto ferrihydrite (Fh_As(V)_coll) (As/Fe=0.09) (synthetic two-line ferrihydrite prepared as in [37]).

The same reference compounds were used for linear least-squares combination fits for Fe EXAFS. Solid lines are data; dashed lines are fits (fit results in Table 3).

8. Element concentrations (mol kg^{-1} sample) in the DCFs (10-1000 nm) and DFs (<10 nm).

Table 1. Dispersible colloid fraction (10-1000 nm) properties (mean ±std dev, n=3)

Sample	WP	RB2	RB	SS	SP
Colloidal mass (mg/ kg sample)	2636±494	840±126	7501±849	4884±710	17645±264
As (mol/ kg colloid)	0.25±0.004	0.08±0.007	0.07±0.015	0.02±0.002	0.01±0.04
Fe (mol/ kg colloid)	0.27±0.014	0.57±0.022	3.97±0.084	0.96±0.128	1.08±2.20
Ca (mol/ kg colloid)	3.55±1.39	0.30±0.066	0.04±0.001	0.15±0.001	0.09±0.28
Al (mol/ kg colloid)	b.d.	1.54±0.076	4.27±0.078	6.57±0.07	4.25±3.99
Cu (mol/ kg colloid)	b.d	b.d	0.02±0.000	0.05±0.002	$2.7\times10^{-3}\pm0.01$
Zn (mol/ kg colloid)	b.d.	$0.01\pm5\times10^{-4}$	$6.9\times10^{-3}\pm1\times10^{-4}$	$5.5\times10^{-3}\pm5\times10^{-5}$	$2.1\times10^{-3}\pm6\times10^{-3}$
Pb (mol/ kg colloid)	$5.3\times10^{-3}\pm1\times10^{-4}$	b.d.	b.d.	b.d.	b.d.
C (mol/ kg colloid)	0.67±0.002	--	0.7±0.002	0.6±0.0092	3.49±0.02

b.d.: below detection limit; --: not detected

Table 2: Arsenic X-ray absorption near edge structure (XANES) and extended X-ray absorption fine structure (EXAFS) fits results.

	Molar As/Fe	XANES (%)[a]	As EXAFS[b]						XRD[c]	
Sample			A-B[d]	N	R (Å)	σ^2 (Å^2)	ΔE_0(Å)	χ^2	N	R (Å)
WP	0.88	a. 61.3 b. 38.7[e]	As-O	4.0[f]	1.69	0.0027[f]	-0.66	3.26		
			MS[g]	1.0	3.07/	0.0050/				
			As-Fe	3.7[f]	3.37	0.0062				
			As-As	0.8[f]	4.22	0.0079				
			As-As	1.9[f]	4.93	0.0089				
RB2	0.16	100.3[h]								
RB	0.016	94.5[h]	As-O	4.0	1.68[c]	0.0023[f]	-1.3	1.37		
			MS[g]	1.0	3.06/	0.0035/				
			As-Fe	1.9[f]	3.32[f]	0.006				
SS	0.027	101.0[h]	As-O	4.0	1.69[f]	0.0024[f]	-0.56	3.7		
			MS[g]	1.0	3.06/	0.0032/				
			As-Fe	0.6[f]	3.40[f]	0.006				
SP	0.013	108.3[h]	As-O	4.0[f]	1.69[f]	0.0028	-1.09	1.36		
			MS[g]	1.0	3.06/	0.0035/				
			As-Fe	1.2[f]	3.31[f]	0.006				
Scorodite[i]	1		As-O	4.0	1.69[f]	0.0027[f]	1.3	1.85	4	1.67-1.69
			MS[g]	1.0	3.07/	0.0050/			2	3.06
			As-Fe	4.0	3.37[f]	0.0062[f]			4	3.37-3.39
			As-As	1.0	4.20[f]	0.0079[f]			1	4.22
			As-As	2.0	4.91[f]	0.0089[f]			2	4.91
			As-As	4.0	5.73[f]	0.0076[f]			4	5.46-5.65
As(V)_Fh[j]	0.012		As-O	4.0[f]	1.68	0.0023	-2.4	1.44		
			MS[g]	1.0	3.06/	0.0035/				
			As-Fe	1.7	3.38	0.006[f]				
			As-Fe	0.8	3.52	0.006[f]				
As(V)_Fh_coll[k]	0.09		As-O	4.0	1.69	0.0033[f]	-0.99	1.07		
			MS[g]	1.0	3.06/	0.0064/				
			As-Fe	1.2[f]	3.28[f]	0.006				

[a]Linear combination fit results for arsenic XANES (fitting range 11850-12000).
[b]Results of As EXAFS shell-by-shell fits for reference compounds and colloids.
[c]Crystallographic distances from from Xu et al. [38].

[d]A–B is the absorber-backscatterer pair; N is the number of backscattering atoms at distance (R); σ^2 (Debye Waller term) is the absorber–backscatterer mean-square relative displacement; ΔE_O is the energy shift in the least-squares fit; χ^2 is a reduced least-squares goodness-of-fit parameter (=(F-factor)/(#points -#variables)); scale factor (S^2_o) fixed at 1.

[e]Fraction corresponded to (a.) scorodite (spectrum from Savage et al.[23], and (b.) arsenate sorbed to hydrous ferric oxide (As(V)_Fh); spectrum from Root et al. [24] and refit in Helmhart et al.[27].

[f]Parameter allowed to vary during the fitting; / parameter linked to the parameter inmediately above in the fitting.

[g]Spectrum fit with multiple scattering path that is a composite of 6 triangular paths (O→O→As).

[h]Fraction corresponded to Arsenate sorbed to hydrous ferric oxide (As(V)_Fh) (%) spectrum from Root et al. [24] and refit in Helmhart et al. [27].

[i]Natural scorodite (FeAsO$_4$ 2H$_2$O) spectrum from Savage et al.[23].

[j]Arsenate sorbed to hydrous ferric oxide (As(V)_Fh); spectrum from Root et al. [24] and refit in Helmhart et al. [27].

[k]Arsenate sorbed to colloidal hydrous ferric oxide (As(V)_Fh_coll) from this study.

Table 3: Linear combination fit results for iron X-ray absorption near edge structure (XANES) and extended X-ray absorption fine structure (EXAFS)

Sample	Fitting range	Scorodite (%)[b]	ΔeV	As_Fh_coll (%)[c]	ΔeV	Smectite (%)[d]	ΔeV	Illlite (%)[e]	ΔeV	Total (%)	red. χ^{2f}
Fe XANES	Energy (eV)										
WP	7105-7160	82.6 / 3.4[g]	0.03	16.4 / 16.6[g]	0.2					99	0.000058
RB2	7105-7160			100	0.2					100	0.000050
RB	7105-7160			62.3 / 60.2[g]	0.39	41.2 / 39.7[g]	-0.2			103	0.000147
SS	7105-7160			44.6 / 43.3[g]	0.02	58.3 / 56.6[g]	-0.09			103	0.000139
SP	7105-7160			39.3 / 39.5[g]	0.04			59.7 / 60[g]	-0.45	99	0.000093

Sample	Fitting range	Scorodite (%)[b]	As_Fh_coll (%)[c]	Smectite(%)[d]	Illlite (%)[e]	Total (%)	red. χ^{2f}
Fe EXAFS	k (Å^{-1})						
WP	2-11	81.9 / 68.8[g]	37.9 / 31.06[g]			119	0.45
RB2	2-11		103.3 / 100[g]			103	0.40
RB	2-11		32 / 41.2[g]	45.6 / 58.7[g]		78	0.50
SS	2-11		34.0 / 42[g]	47 / 58[g]		81	0.30
SP	2-11		25.2 / 27[g]		68.1 / 73[g]	93	0.93

[b]Fit with natural scorodite spectrum from Savage et al. [23] /and fit in this study (Table EA-7).

[c]Fit with As(V)_Fh_coll spectrum synthesized and analyzed in this study (Fig. 7, Table 9).

[d]Fit with reference smectite (SAz-1), Clay Minerals Society reference mineral previously analyzed by O´Day et al. [25]

[e]Fit with reference illite (IMt-1), Clay Minerals Society reference mineral previously analyzed by O´Day et al. [25]

[f]Goodness-of fit reported as reduced χ^2 calculated as three times the estimated standard deviation for each component from the linear least-squares fit.

[g]Recalculated to Total 100%

20

REFERENCES

[1] R. Kretzschmar, M. Borkovec, D. Grolimund, M. Elimelech, Mobile subsurface colloids and their role in contaminant transport, Adv Agron. 66, (1999) 121-193.

[2] R. Kretzschmar, T. Schafer, Metal retention and transport on colloidal particles in the environment, Elements, 1 (2005) 205-210.

[3] A.D. Karathanasis, D.M.C. Johnson, Subsurface transport of Cd, Cr, and Mo mediated by biosolid colloids, Sci. Tot. Environ. 354 (2006) 157-169.

[4] M. Hassellöv, K.O. Buesseler, S.M. Pike, M. Dai, Application of cross-flow ultrafiltration for the determination of colloidal abundances in suboxic ferrousrich ground waters, Sci. Tot. Environ. 372 (2007) 636-644.

[5] M. Bauer, C. Blodau, Arsenic distribution in the dissolved, colloidal and particulate size fraction of experimental solutions rich in dissolved organic matter and ferric iron, Geochim. Cosmochim. Acta 73 (2009) 529-542.

[6] P. Sharma, J. Ofner, A. Kappler, Formation of Binary and Ternary Colloids and Dissolved Complexes of Organic Matter, Fe and As, E Environ. Sci. Technol. 44 (2010) 4479-4485.

[7] K. Tindale, P. Patel, D. Wallschläger, Colloidal arsenic composition from abandoned gold mine tailing leachates in Nova Scotia, Canada, App. Geochem. 26(2011) S260-S262..

[8] J.-M. Séquaris, E. Klumpp, H. Vereecken, Colloidal properties and potential release of water-dispersible colloids in an agricultural soil depth profile, Geoderma, 193–194 (2013) 94-101.

[9] C. Jiang, J.M. Séquaris, H. Vereecken, E. Klumpp, Diffusion-controlled mobilization of water-dispersible colloids from three German silt loam topsoils: effect of temperature, Eur. J. Soil Sci. 64 (2013) 777-786.

[10] R. Kretzschmar, H. Sticher, Transport of Humic-Coated Iron Oxide Colloids in a Sandy Soil:Influence of $Ca2+$ and Trace Metals, E Environ. Sci. Technol. 31 (1997) 3497-3504.

[11] C. Kjaergaard, Colloid mobilization and transport in structured soils, Ph.D. Dissertation, Department of Environmental Engineering, Aalborg University, 2004.

[12] S. Dubascoux, I. Le Hécho, M. Potin Gautier, G. Lespes, On-line and off-line quantification of trace elements associated to colloids by As-Fl-FFF and ICP-MS, Talanta, 77 (2008) 60-65.

[13] E. Bolea, F. Laborda, J.R. Castillo, Metal associations to microparticles, nanocolloids and macromolecules in compost leachates: Size characterization by asymmetrical flow field-flow fractionation coupled to ICP-MS, Anal. Chim. Acta, 661 (2010) 206-214.

[14] M. Plaschke, T. Schafer, T. Bundschuh, T.N. Manh, R. Knopp, Size characterization of bentonite colloids by different methods, Anal. Chem. 73 (2001) 4338-4347.

[15] F. Von der Kammer, M. Baborowski, S. Tadjiki, W. Von Tumpling, Colloidal particles in sediment pore waters: Particle size distributions and associated element size distribution in anoxic and re-oxidized samples, obtained by FFF-ICP-MS coupling, Acta Hydrochim. Hydrobiol. 31 (2004) 400-410.

[16] A.J. Slowey, S.B. Johnson, M. Newville, G.E. Brown Jr, Speciation and colloid transport of arsenic from mine tailings, AppGeochem. 22 (2007) 1884-1898.

[17] H. Zänker, H. Moll, W. Richter, V. Brendler, C. Hennig, T. Reich, A. Kluge, G. Hüttig, The colloid chemistry of acid rock drainage solution from an abandoned Zn-Pb-Ag mine, App Geochem. 17 (2002) 633-648.

[18] K.L. Haus, R.L. Hooper, L.A. Strumness, J.B. Mahoney, Analysis of arsenic speciation in mine contaminated lacustrine sediment using selective sequential extraction, HR-ICPMS and TEM, App. Geochem., 23 (2008) 692-704.

[19] L. Recio-Vazquez, J. Garcia-Guinea, P. Carral, A. Alvarez, F. Garrido, Arsenic Mining Waste in the Catchment Area of the Madrid Detrital Aquifer (Spain), Water Air Soil Poll. 214 (2011) 307-320.

[20] F. Laborda, S. Ruiz-Begueria, E. Bolea, J.R. Castillo, Study of the size-based environmental availability of metals associated to natural organic matter by stable isotope exchange and quadrupole inductively coupled plasma mass spectrometry coupled to asymmetrical flow field flow fractionation, J. Chromatogr. A, 1218 (2011) 4199-4205.

[21] B. Ravel, ATHENA User'sGuide 1.5, 2009.

[22] G.N. George, I.J. Pickering, EXAFSPAK: A suite of computer programs for analysis of X-ray absorption spectra, Stanford Syncrotron Radiation Laboratory, 2000.

[23] K.S. Savage, D.K. Bird, P.A. O'Day, Arsenic speciation in synthetic jarosite, Chemi. Geol.215 (2005) 473-498.

[24] R.A. Root, D. Vlassopoulos, N.A. Rivera, M.T. Rafferty, C. Andrews, P.A. O'Day, Speciation and natural attenuation of arsenic and iron in a tidally influenced shallow aquifer, Geochim. Cosmochim. Acta, 73 (2009) 5528-5553.

[25] P.A. O'Day, N. Rivera, Jr., R. Root, S.A. Carroll, X-ray absorption spectroscopic study of Fe reference compounds for the analysis of natural sediments, Am. Mineral. 89 (2004) 572-585.

[26] D. Paktunc, K. Bruggeman, Solubility of nanocrystalline scorodite and amorphous ferric arsenate: Implications for stabilization of arsenic in mine wastes, AppGeochem. 25 (2010) 674-683.

[27] M. Helmhart, P. O´Day, J. Garcia-Guinea, S. Serrano, F. Garrido, Arsenic, Copper, and Zinc Leaching through Preferential Flow in Mining-Impacted Soils, Soil Sci. Soc. Am. J. 76 (2012) 449-462.

[28] D.A. Dzombak, M.M. Morel F, Surface Complexation Modelling: Hydrous Ferric Oxide, Wiley-Interscience,, New York, 1990.

[29] S. Serrano, P.A. O'Day, D. Vlassopoulos, M.T. Garcia-Gonzalez, F. Garrido, A surface complexation and ion exchange model of Pb and Cd competitive sorption on natural soils, Geochim. Cosmochim. Acta 73 (2009) 543-558.

[30] C. Neal, S. Lofts, C.D. Evans, B. Reynolds, E. Tipping, M. Neal, Increasing Iron Concentrations in UK Upland Waters, Aquat.Geochem. 14 (2008) 263-288.

[31] E. Neubauer, W.D.C. Schenkeveld, K.L. Plathe, C. Rentenberger, F. von der Kammer, S.M. Kraemer, T. Hofmann, The influence of pH on iron speciation in podzol extracts: Iron complexes with natural organic matter, and iron mineral nanoparticles, Sci. Tot. Environ. 461–462 (2013) 108-116.

[32] J.F. McCarthy, J.M. Zachara, Subsurface transport of contaminants, Environmental Science & Technology, 23 (1989) 496-502.

[33] T. Areepitak, J. Ren, Model Simulations of Particle Aggregation Effect on Colloid Exchange between Streams and Streambeds, Environmental Science & Technology, (2011).

[34] M. Stumm, Chemistry of the Solid-Water Interface, John Wileny & Sons, New York, 1996.

[35] M. Hassellov, F. von der Kammer, Iron Oxides as Geochemical Nanovectors for Metal Transport in Soil-River Systems, Elements, 4 (2008) 401-406.

[36] S. Dixit, J.G. Hering, Comparison of Arsenic(V) and Arsenic(III) Sorption onto Iron Oxide Minerals: Implications for Arsenic Mobility, Environ. Sci.Technol. 37 (2003) 4182-4189.

[37] U. Schwertmann, R.M. Cornell, Iron oxides in the laboratory: Preparation and characterization, WILEY-VCH Verlag GmbH, Weinheim, Germany, 2007.

[38] Y. Xu, G.-P. Zhou, X.-F. Zheng, Redetermination of iron(III) arsenate dihydrate, Acta Crystallogr. E 63 (2007) i67-i69.
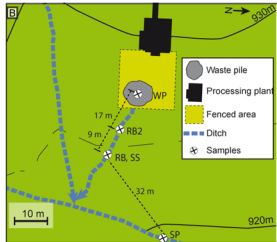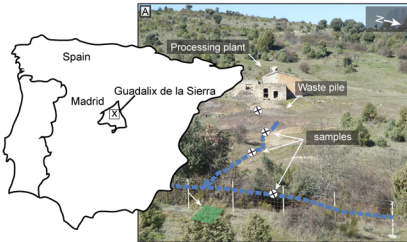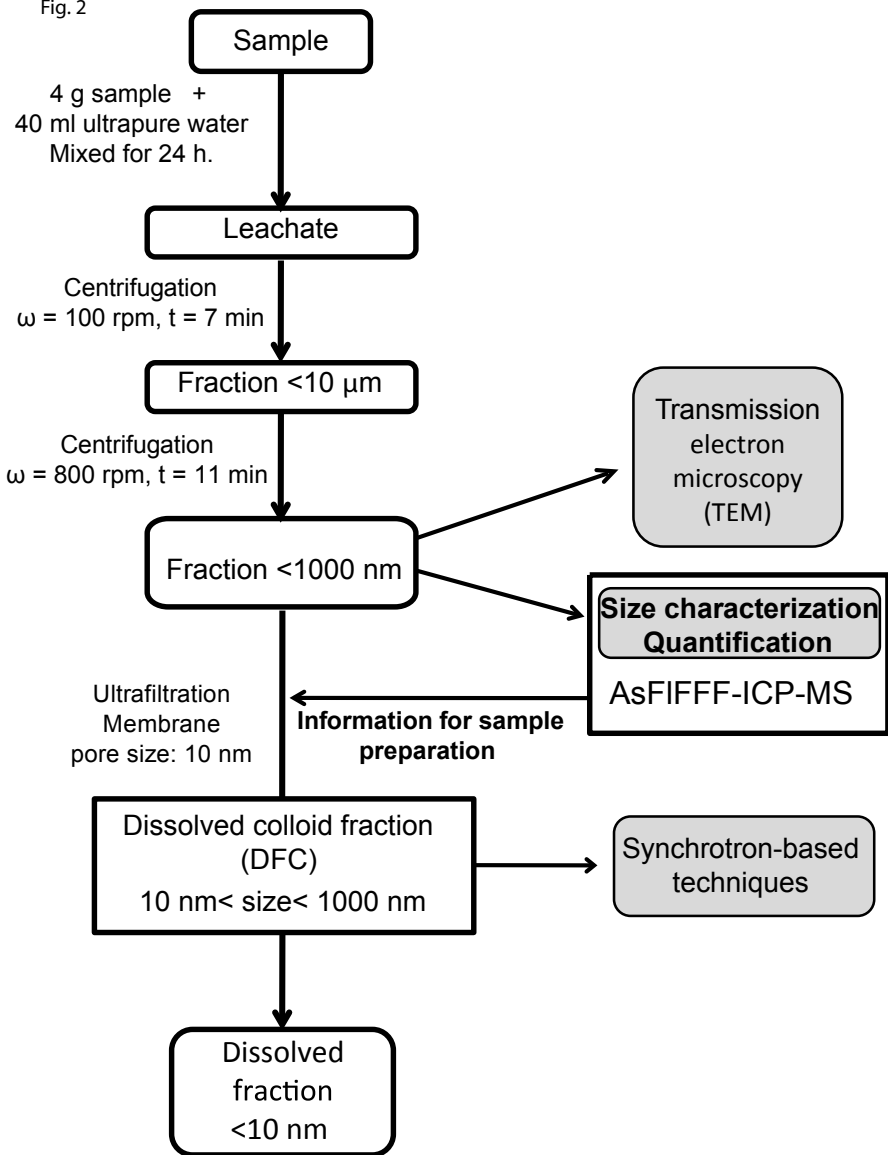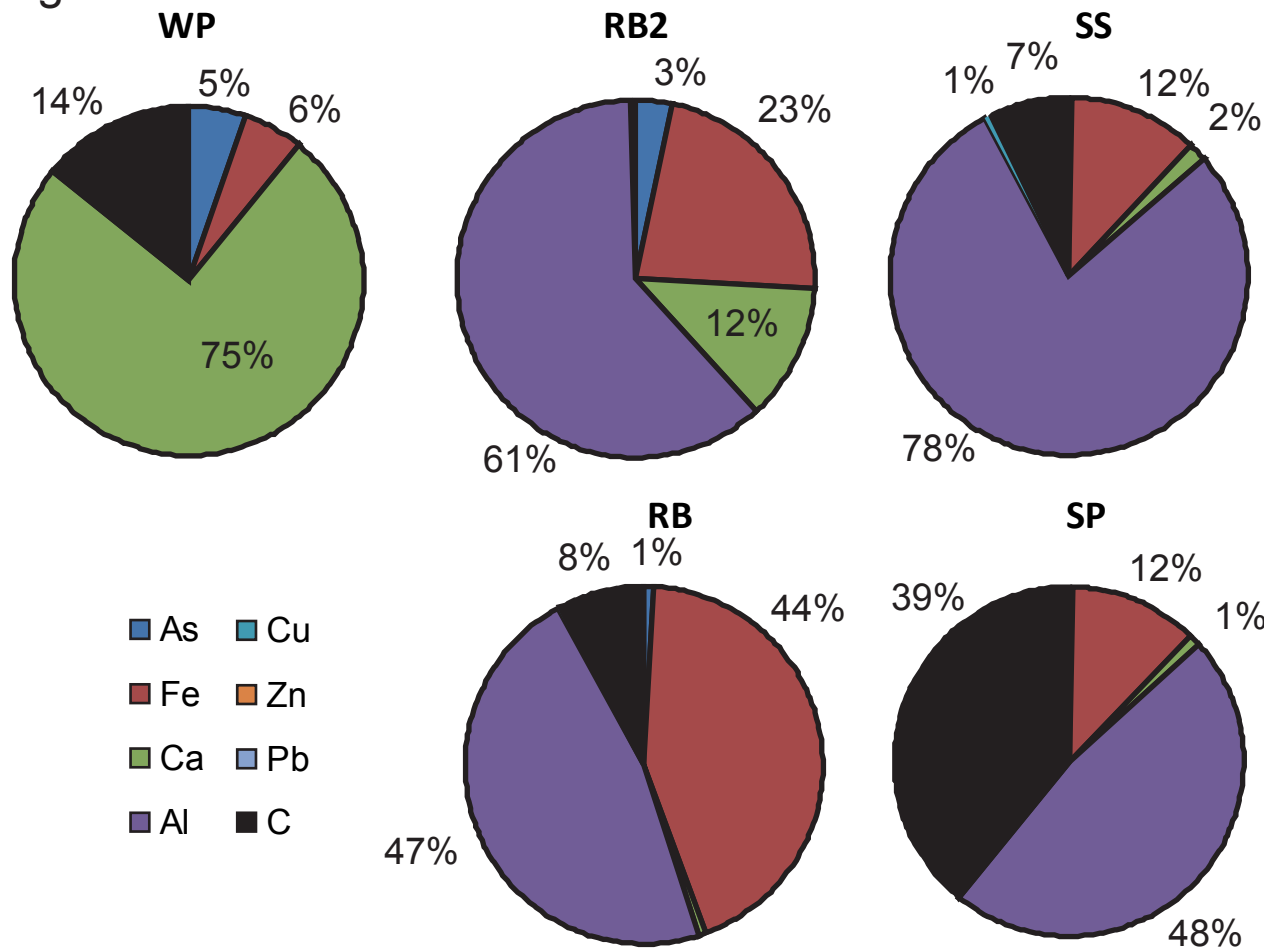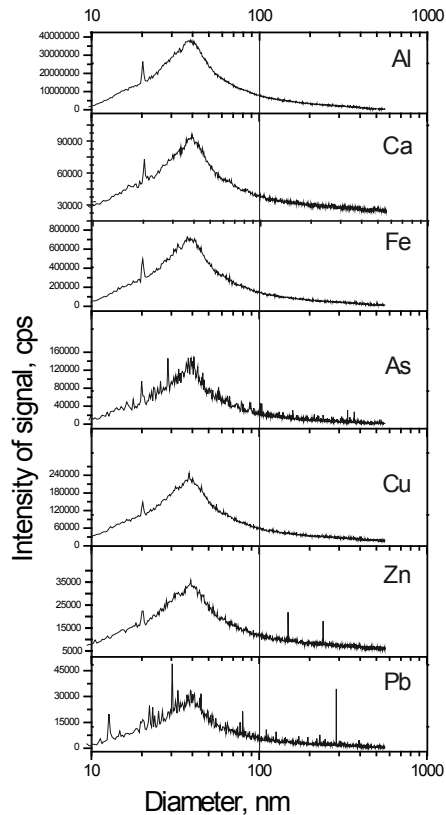
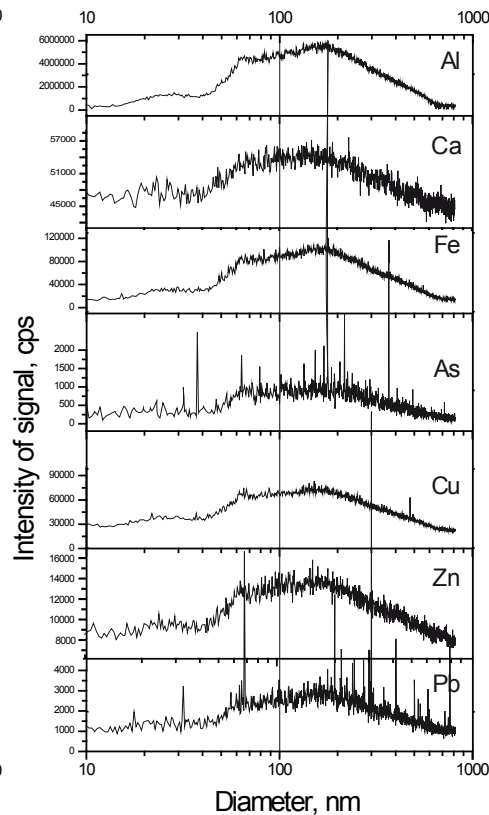Fig. 1

Fig. 2

Fig. 3

Fig. 4

a) RiverBed (RB) b) SubSoil (SS) c) Sediment pond (SP)
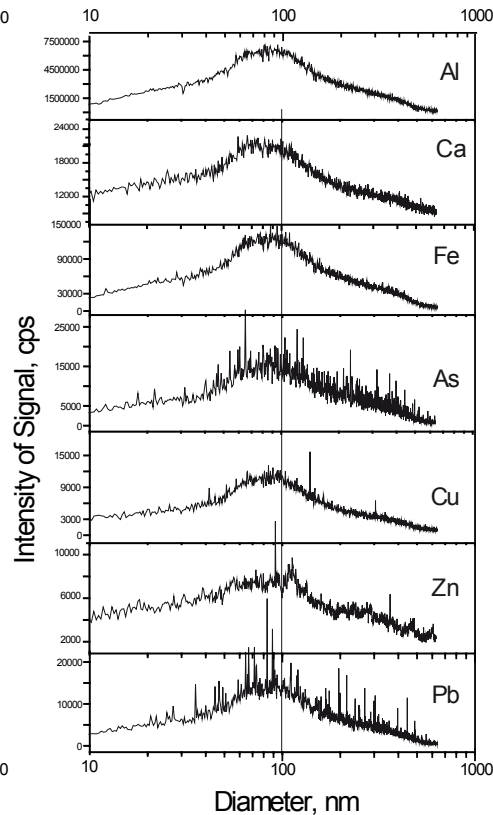
Fig. 5

a) Wastepile (WP) — Scorodite — 80 nm

b) RiverBed_2 (RB2) — 50 nm

c) RiverBed (RB) Fe-particle — 10 nm

d) RiverBed (RB) — 50 nm

e) Subsoil (SS) Fe-particle — 5 nm

f) Sediment Pond (SP) — 10 nm
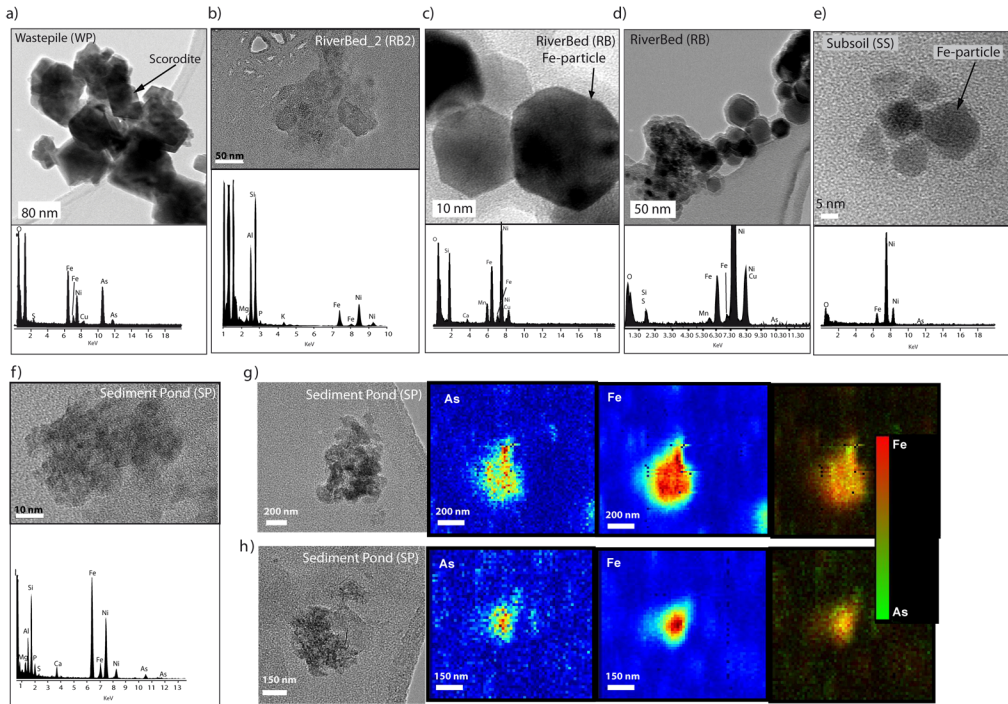
g) Sediment Pond (SP) — As / Fe / Fe-As — 200 nm

h) Sediment Pond (SP) — As / Fe / Fe-As — 150 nm

As XANES
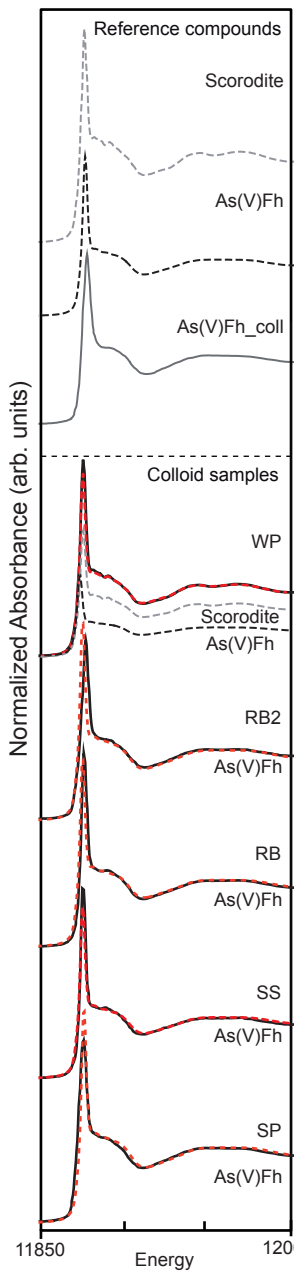
As EXAFS

Fourier Transform

Reference compounds

Scorodite

As(V)Fh

As(V)Fh_coll

Colloid samples

WP

Scorodite

As(V)Fh

RB2

As(V)Fh

RB

As(V)Fh

SS

As(V)Fh

SP

As(V)Fh

Scorodite

As(V)Fh

As(V)Fh_coll

WP

RB

SS

SP

O

Fe

As

O

Fe

Fe

O

Fe

O

Fe

As

O

Fe

O

Fe

O

Fe
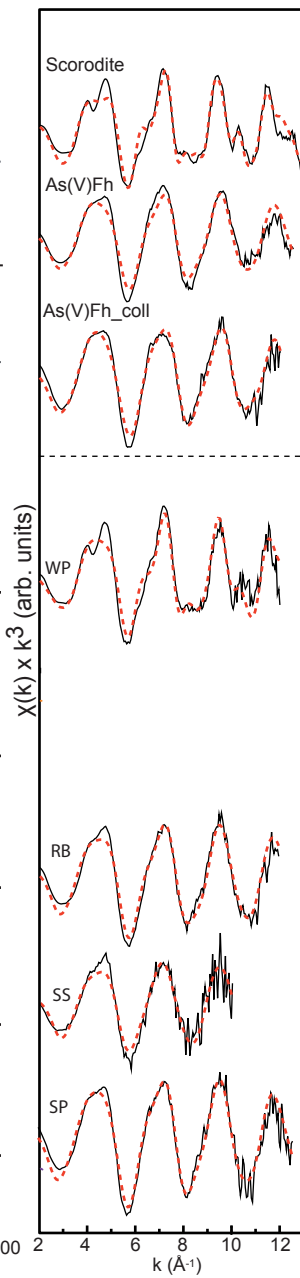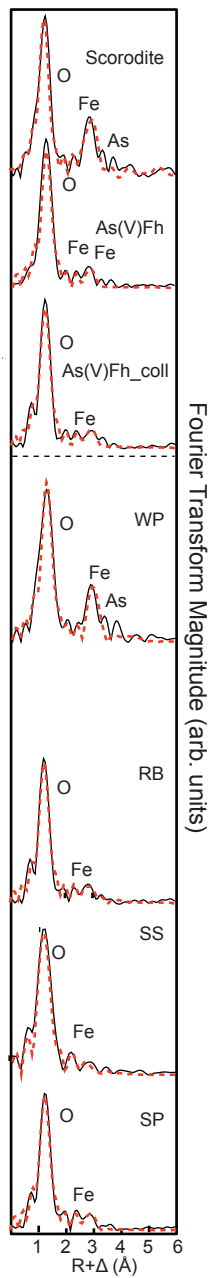
Normalized Absorbance (arb. units)
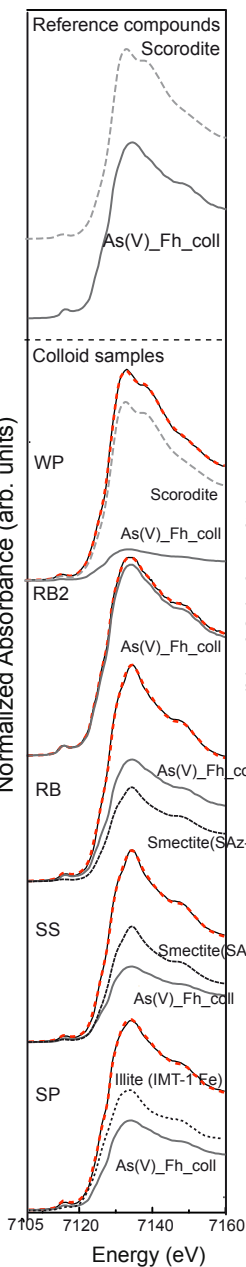
$\chi(k) \times k^3$ (arb. units)

Fourier Transform Magnitude (arb. units)

11850   Energy   12000

2   4   6   8   10   12
k (Å⁻¹)

1   2   3   4   5   6
R+Δ (Å)

Fe XANES

Reference compounds
Scorodite
As(V)_Fh_coll

Colloid samples

WP
Scorodite
As(V)_Fh_coll

RB2
As(V)_Fh_coll

RB
As(V)_Fh_coll
Smectite(SAz-1)

SS
Smectite(SAz-1)
As(V)_Fh_coll

SP
Illite (IMT-1 Fe)
As(V)_Fh_coll

Normalized Absorbance (arb. units)

Energy (eV)

Fe EXAFS

Scorodite
As(V)_Fh_coll
WP
RB2
RB
SS
SP

χ(k) x k3 (arb. units)

k (Å-1)

Fourier Transform

Scorodite
As(V)_Fh_coll
WP
RB2
RB
SS
SP

Fourier Transform Magnitude (arb. units)

R+Δ (Å)

Fig. 8

Appendix A. Supplementary data

Arsenic speciation in the dispersable colloidal fraction of soils from a mine-impacted creek

Susana Serrano[a], Miguel Angel Gomez-Gonzalez[b] , Peggy A. O'Day[c], Francisco Laborda[d], Eduardo Bolea[d], and Fernando Garrido[b].

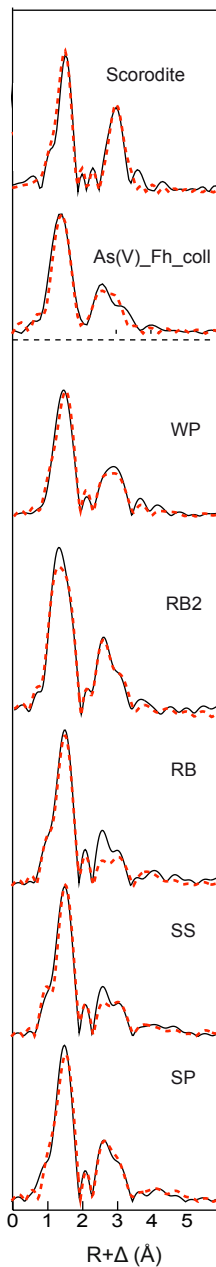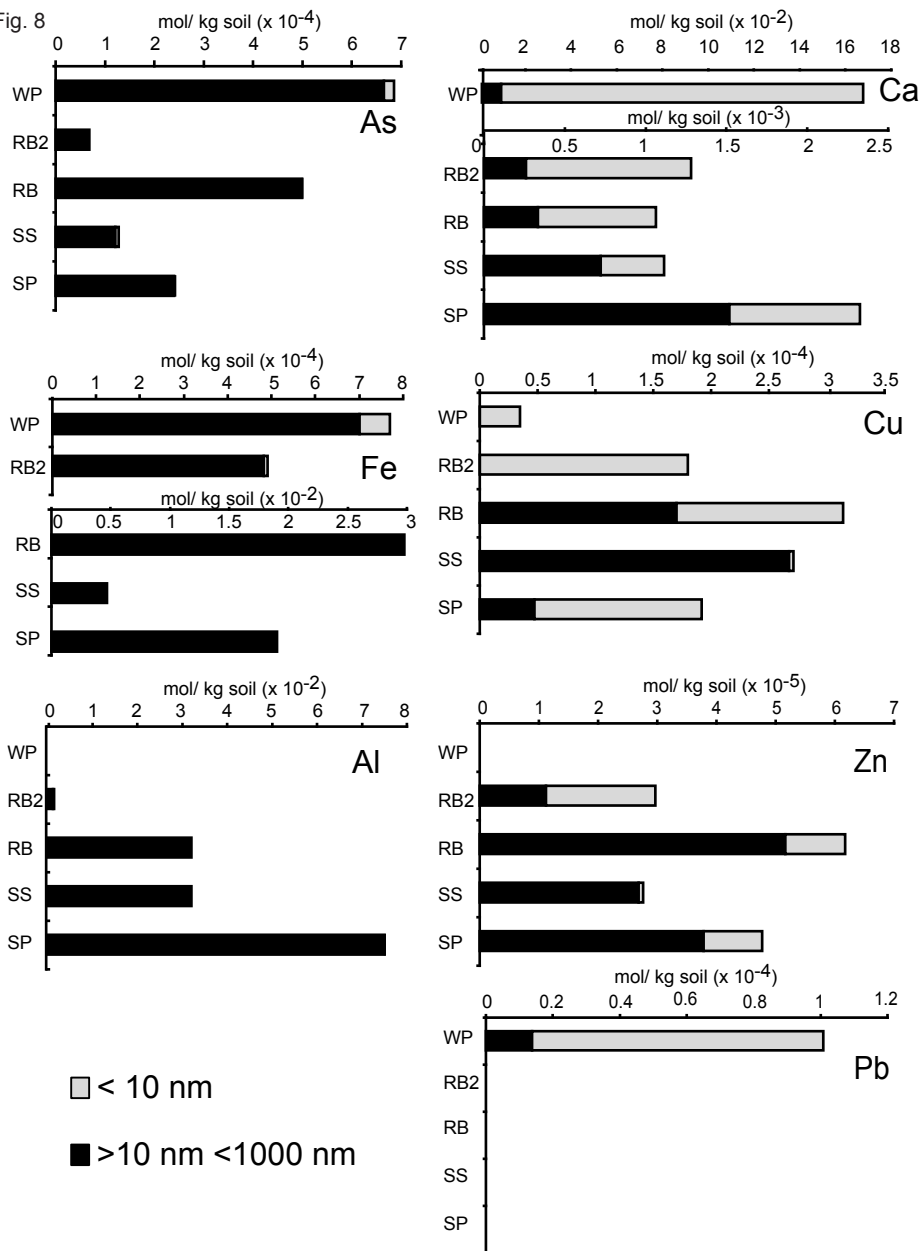[a]Institute of Agrochemistry and Food Technology, CSIC. Agustín Escardino, 7. 46980 Paterna Valencia, Spain

[b]National Museum of Natural Sciences, CSIC, José Gutiérrez Abascal 2, 28006 Madrid, Spain

[c]School of Natural Sciences, University of California, Merced, CA 95343, USA

[d] Group of Analytical Spectroscopy and Sensors (GEAS), Institute of Environmental Sciences (IUCA), University of Zaragoza, Pedro Cerbuna 12, 50009 Zaragoza, Spain

Supplemental Information on Experimental Methods: Description of the methods used for characterization of bulk samples, AsFlFFF procedures (Steric inversion, channel calibration and recoveries), TEM and Microfocused-XRF methods, As and Fe XAS data collection and analysis, and reference compounds

Figure EA-1. X-ray diffractograms of bulk samples

Table EA-1. Physical and chemical properties of the bulk samples

Table EA-2. Crossflow program for AsFlFFF separation.

Table EA-3. ICP-MS instrumental and data acquisition parameters

Table EA-4. Element recoveries from AsFlFFF-ICP-MS

Table EA-5. Element concentration in the dissolved (< 10 nm) fraction.

1. Methods for bulk sample characterization

Soil pH was measured in deionized water (pH_w) and in 1 M KCl (pH_K) (in a 1:5 suspension). Electrical conductivity (EC) was measured in a 1:5 suspension. The exchangeable bases were extracted with 1 M ammonium acetate (NH_4OAc), pH 7 [1] and the exchangeable aluminium (AlK) was extracted with 1 M KCl [2]. The effective cation exchange capacity (ECEC) was calculated as the sum of AlK and the amounts of Ca, Mg, Na and K extracted by 1M NH_4OAc at pH 7 [3]. Soil organic carbon (OC) content was determined by wet digestion [4]. Total As, Fe, Al and S concentrations were determined by dissolving the samples in aqua regia followed by analysis using inductively coupled plasma-optical emission spectrometry (ICP-OES) on a Perkin-Elmer OPTIMA 4300DV (Perkin-Elmer, Germany). The bulk mineralogy of each tailing size fraction was determined by powder X-ray diffraction (XRD) (X'Pert- MPD, PANalytical – Spectrics, UK). The organic carbon concentration was determined by wet digestion [4].
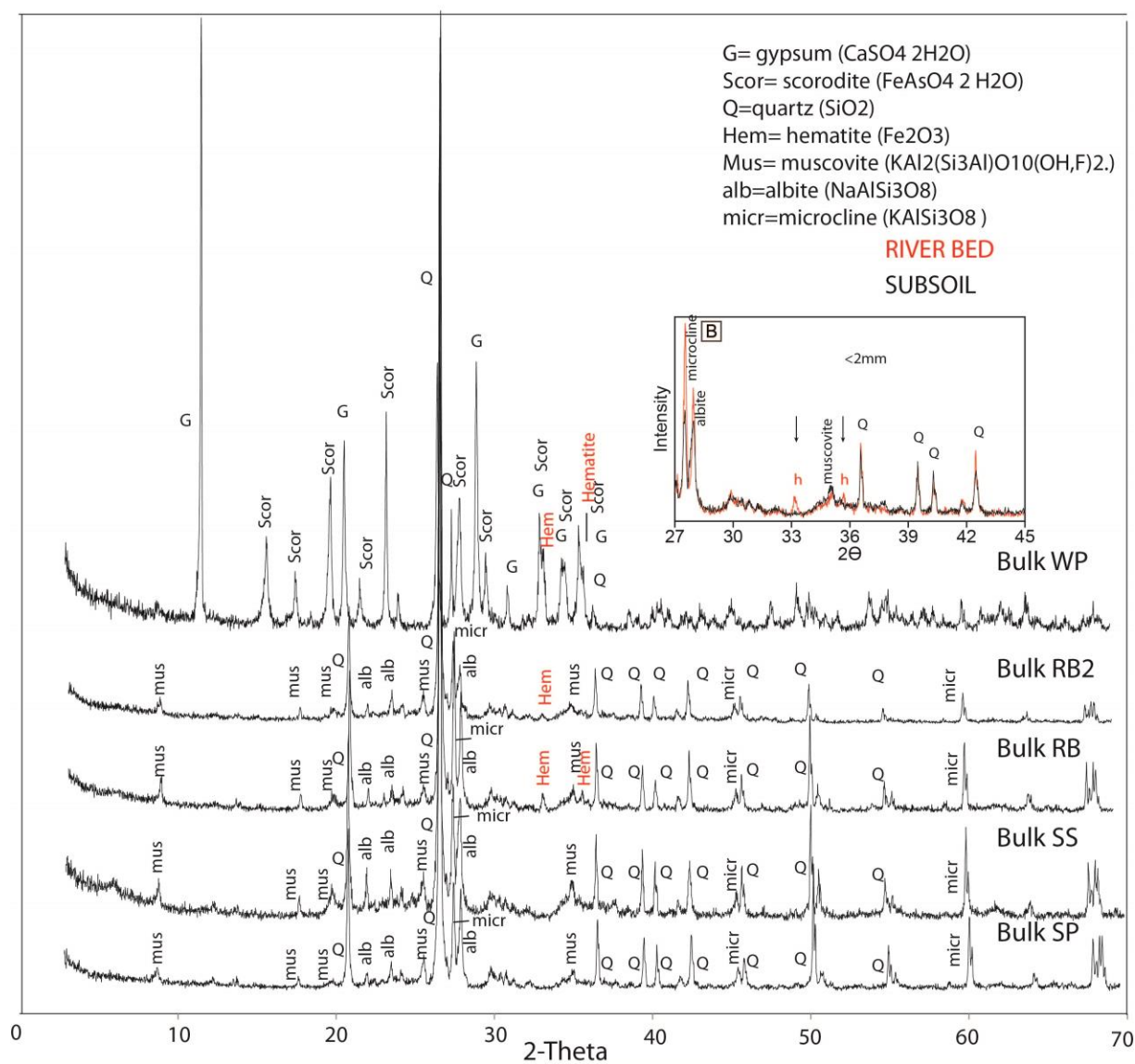
Figure EA-1. X-ray diffractograms of bulk samples from the wastepile (WP), riverbed (RB2 and RB), subsoil (SS), and sediment pond (SP). A magnified section is showed to emphasize the primary reflections from hematite in the riverbed samples (RB2 and RB).

Table EA-1. Physical and chemical properties of bulk samples (mean values, n = 3 ± RSD).

Samples[a]	WP	RB2	RB	SS	SP
Depth (cm)	0-20	0-5	0-10	10-20	0-5
pH_w[b]	3.3	3.9	4.3	4.5	6.2
pH_k[c]	3.1	3.2	3.6	3.6	4.8
EC (uS/cm)	2330	121.5	55.2	58.8	40.7
OC^d (g/kg)	b.d	3.6	8.8	b.d	9.0
$ECEC^e$ (eq/kg)	0.79	0.06	0.11	0.19	0.05
K (mol/kg)	4.4×10^{-4}	8.3×10^{-3}	1.6×10^{-3}	2.4×10^{-3}	2.2×10^{-3}
Ca (mol/kg)	3.9×10^{-1}	4.9×10^{-3}	6.1×10^{-3}	1.3×10^{-2}	1.6×10^{-2}
Na (mol/kg)	3.6×10^{-4}	1.1×10^{-3}	3.7×10^{-3}	4.7×10^{-4}	1.7×10^{-3}
Mg (mol/kg)	1.7×10^{-4}	9.8×10^{-4}	1.8×10^{-3}	5.7×10^{-3}	5.2×10^{-3}
Al (mol/kg)	2.6×10^{-4}	1.3×10^{-2}	3.1×10^{-2}	4.9×10^{-2}	6.9×10^{-4}
Total element composition[f]					
As (mol/kg)	$1.8 \pm 2 \times 10^{-5}$	$3.2 \times 10^{-2} \pm 2 \times 10^{-6}$	$1.4 \times 10^{-3} \pm 7 \times 10^{-5}$	$1.3 \times 10^{-3} \pm 2 \times 10^{-5}$	$2.3 \times 10^{-3} \pm 2 \times 10^{-5}$
Fe (mol /kg)	$3.5 \pm 2 \times 10^{-5}$	$0.65 \pm 3 \times 10^{-6}$	$0.48 \pm 4 \times 10^{-5}$	$0.48 \pm 2 \times 10^{-5}$	$0.37 \pm 1 \times 10^{-5}$
S (mol/kg)	$1.3 \pm 8 \times 10^{-5}$	$1.7 \times 10^{-2} \pm 7 \times 10^{-6}$	$6.1 \times 10^{-3} \pm 1 \times 10^{-5}$	$3.4 \times 10^{-3} \pm 7 \times 10^{-5}$	$4.7 \times 10^{-3} \pm 3 \times 10^{-5}$
Ca (mol/kg)	$1.1 \pm 3 \times 10^{-5}$	$1.5 \times 10^{-2} \pm 2 \times 10^{-5}$	$3.5 \times 10^{-2} \pm 6 \times 10^{-5}$	$3.5 \times 10^{-2} \pm 3 \times 10^{-5}$	$3.5 \times 10^{-2} \pm 3 \times 10^{-5}$
Cu (mol/kg)	$2.1 \times 10^{-2} \pm 5 \times 10^{-6}$	$3.2 \times 10^{-3} \pm 7 \times 10^{-6}$	$9.9 \times 10^{-3} \pm 3 \times 10^{-5}$	$9.3 \times 10^{-3} \pm 2 \times 10^{-5}$	$8 \times 10^{-4} \pm 7 \times 10^{-6}$
Pb (mol/kg)	$3.7 \times 10^{-3} \pm 8 \times 10^{-6}$	$1.7 \times 10^{-4} \pm 2 \times 10^{-5}$	$1.1 \times 10^{-4} \pm 4 \times 10^{-5}$	$9.6 \times 10^{-5} \pm 5 \times 10^{-5}$	$1.3 \times 10^{-4} \pm 3 \times 10^{-5}$
Zn (mol/kg)	$2.4 \times 10^{-3} \pm 2 \times 10^{-5}$	$1.5 \times 10^{-3} \pm 1 \times 10^{-6}$	$2.1 \times 10^{-3} \pm 9 \times 10^{-6}$	$2.1 \times 10^{-3} \pm 6 \times 10^{-6}$	$1.2 \times 10^{-3} \pm 2 \times 10^{-5}$
Mineralogical composition[g]					
Major phases					
	Quartz	Quartz	Quartz	Quartz	Quartz
	Scorodite				
		Feldspar	Feldspar	Feldspar	Feldspar
	Gypsum				
		Albite	Albite	Albite	Albite
		Muscovite	Muscovite	Muscovite	
Minor phases					
	Hematite	Hematite	Hematite		Muscovite

[a] WP= Waste Pile, RB2=Riverbed #2, RB=Riverbed, SS=Subsoil, SP=sediment pond; nd= not detected
[b] pH_w, pH measured in deionized water
[c] pH_k, pH measured in 1 M KCl
EC: Electrical conductivity
[d] Organic carbon [4]
[e] ECEC=Effective cation exchange capacity as the sum of Ca, Mg, Na, K and Al [3]
[f] Microwave digestion in aqua regia and analysis by ICP-OES
[g] XRD analysis
b.d. below detection

2. Dispersible colloid fraction: preparation and pre-fractionation

After passage of the air-dried samples though a 4 mm sieve, 4 g were placed in 50 ml

polyethylene tubes with 40 ml of ultrapure water (performed in duplicate). The resulting slurries

were mixed at room temperature using a rotary tumbler at 28±2 rpm. After 24 h, the pH and conductivity of the supernatants were measured. Particles larger than 10 μm were then removed by centrifugation at 100 rpm for 7 min in a Heraeus Multifuge X1 device equipped with a TX-400 rotor (Thermo Scientific). This suspension was then further centrifuged at 800 rpm for 11 min to isolate the <1000 nm fraction. Finally, the dissolved fraction (DF) was obtained from the collected <1000 nm fraction by ultrafiltration through a Microsep Omega 100 kDa ultrafiltration membrane (Pall Filtron) with a nominal pore size of 10 nm. Measurements of the suspension ultrafiltrates by an AF2000 AsFlFFF apparatus (Postnova Analytics) showed no DCF of <10 nm (see below). Colloids between 10 nm and 1000 nm (DCF) were retained on the ultrafiltration membrane and stored for further analysis.

3. AsFlFF-ICP-MS

3.1. Steric inversion and channel calibration

According to the FFF theory, in normal mode it is possible to establish a relationship between the retention ratio (R) and the diffusion coefficient (D) of the eluted species, which can be related to their hydrodynamic diameter (d) using the Stokes-Einstein equation [5]. In steric mode, however, the relationship between the retention ratio R is more complex and depends on several conditions [6].

A different approach to the problem can be done by obtaining the experimental relationship between the retention ratio and size using a set of size standards [6]. In this case, a similar behaviour between the size standards and the particles to be characterized has to be assumed. This approach has been followed in the present work and a set of silica dioxide (SiO_2) standards has been used because of its similarity to the unknown samples. Monodispersed silica dioxide microparticles having standardized sizes (0.020 ± 0.004, 0.15 ± 0.03, 0.5 ± 0.05, 1 ±

0.05, 2 ± 0.08, 5 ± 0.1 µm) were used for AsFlFFF calibration applying the crossflow program described in the Table 1 of the manuscript. The steric inversion point was calculated according to the following equations of the calibration curves obtained with these standards:

normal mode: $\log R = -2.1298 - 0.7854 \log d$, $r = 0.992$

steric mode: $\log R = -2.0384 + 0.7146 \log d$, $r = 0.987$

where d is the particle diameter (µm) and $R = t_0/t_r$, where t_0 is the elution time corresponding to the void volume and t_r is the retention time for a given particle. An inversion point of 0.87 µm was obtained by the intersection of the two curves.

Standards were purchased from Sigma-Aldrich (Sigma-Aldrich Chemie, Switzerland). Diluted solutions (20 mg L^{-1}) of these standards were prepared by further dilution with the corresponding mobile phase. Elution was monitored by UV-Vis at 254, 400 and 600 nm.

2.2. Recovery calculations

Recovery calculations were made using three injections of sample without applying any crossflow in the AsFlFFF channel (no injection step was applied either). Then, injections applying the crossflow program described in Table 1 of the manuscript were carried out. Afterwards peaks areas were calculated from signal and the recoveries expressed as:

$R(\%) = S/S_0 \times 100$

where S is the signal area obtained when a crossflow is applied, and S_0 is the signal area obtained with no crossflow. In general, low recoveries are associated with adsorption processes of the species injected onto the permeation membrane of the channel, or with losses by filtration through the membrane of those species with molecular weight lower than its pore size (< 1 kDa). Recoveries were calculated both from the absorbance signal at 600 nm and the ICP-MS signals (Table EA-3).

Table EA-2: Crossflow program for AsFlFFF separation.

	Carrier	Time (min)	Cross flow type	Cross flow (mL min^{-1})
Program 1 colloids	Ultrapure water pH 0.01 % SDS 4.5^a or pH 6.5^b	35 3 2	*Constant* *Linear Decay* *Constant*	0.1 0 0

Outflow 0.8 mL min^{-1}
^{a} For RB and SS samples
^{b} For SP sample

Table EA-3. ICP-MS instrumental and data acquisition parameters.

Instrumental parameters	
RF Power	1200 W
Argon gas flow rate	
Plasma	15 L min^{-1}
Auxiliary	1.2 L min^{-1}
Nebulizer	0.9 L min^{-1}

Data acquisition parameters	
Measuring mode	Peak hopping
Points per spectral peak	1
Dead time	60 ns
Sweeps	10
Dwell time	5 ms
Integration time per point	50 ms
Settle Time	3 ms

Table EA-4: Recoveries for target metals in the measured samples from AsFlFFF-ICP-MS fractograms (**%**).

	Samples				
Element	WP^a	RB2^a	RB	SS	SP
UV-vis at 600 nm	-	-	73.1	64.2	71.6
As	-	-	75.0	54.0	63.5
Fe	-	-	96.8	63.7	78.9
Al	-	-	77.5	59.8	74.9
Pb	-	-	86.8	64.3	77.0

^{a}Not measured by AsFlFFF-ICP-MS

Table EA-5. Element concentration (mmol/ Kg sample)in the dissolved (< 10 nm) fraction. (mean values, n = 3 ± SD).

	WP	RB2	RB	SS	SP
As	$0.02 \pm 2.6 \times 10^{-4}$	b.d.	$0.001 \pm 4 \times 10^{-5}$	$0.007 \pm 1 \times 10^{-4}$	$0.002 \pm 8.1 \times 10^{-5}$
Fe	$0.06 \pm 1.2 \times 10^{-3}$	$0.08 \pm 1.4 \times 10^{-3}$	b.d.	b.d.	b.d.
Ca	158.2 ± 1.77	$1.02 \pm 2.8 \times 10^{-2}$	$0.73 \pm 1.9 \times 10^{-2}$	$0.39 \pm 1.4 \times 10^{-2}$	$0.80 \pm 1.7 \times 10^{-2}$
Al	b.d.	$0.22 \pm 2.2 \times 10^{-3}$	$0.06 \pm 5.5 \times 10^{-4}$	$0.009 \pm 2.2 \times 10^{-4}$	$10.06 \pm 8.2 \times 10^{-4}$
Cu	$0.03 \pm 3.1 \times 10^{-4}$	$0.18 \pm 1.2 \times 10^{-3}$	$0.14 \pm 7.8 \times 10^{-4}$	$0.003 \pm 4.7 \times 10^{-4}$	$0.14\ 1.6 \times 10^{-3}$
Zn	b.d.	$0.02 \pm 1.4 \times 10^{-4}$	$0.01 \pm 1.8 \times 10^{-4}$	$0.0007 \pm 3.5 \times 10^{-5}$	$0.009 \pm 1.5 \times 10^{-4}$
Pb	$0.08 \pm 9.1 \times 10^{-4}$	b.d.	b.d.	b.d.	b.d.

b.d. below detection limit

4. Transmission electron microscopy

Aliquots of the <1000 nm fraction from the WP, RB and SS samples were deposited on carbon-coated Ni grids and examined using a CM200FEG transmission electron microscope (TEM) (Philips, Netherlands) at an operating voltage of 200 kV (resolution 0.24 nm). Energy-dispersive X-ray (EDX) analysis was performed with an EDAX DX-4 system (EDAX, USA). Aliquots of the <1000 nm fraction from the RB2 and SP samples were deposited on carbon-coated Ni grids and examined using a JEOL JEM-2100 TEM (Jeol, Japan) at an operating voltage of 200 kV. EDX analysis was performed with an OXFORD INCA system (Oxford Instruments, UK).

5. Microfocused synchrotron X-ray fluorescence

Chemical mapping was performed on the <1000 nm SP fraction using synchrotron microfocused X-ray fluorescence (μXRF) at the Stanford Synchrotron Radiation Lightsource (SSRL) laboratory (on Beamline 2-3) at room temperature using a Si(220) double crystal monochromator and a single-element Si Vortex detector. Suspension aliquots were deposited on adhesive tape and allowed to dry. The X-ray energy was tuned to 12500 eV and fluorescence maps were collected in continuous raster scanning mode for As, Ca, Fe, Cu and

Zn. The maps were analyzed using Microanalysis Toolkit software [21]; element count rates were normalized to the measured intensity of the incident X-ray beam (I_0).

6. X-ray Absorption Spectroscopy (XAS)

6.1. XAS data collection

Arsenic and Fe K-edge spectra of DCF samples (on their ultrafiltration membrane), and of a reference DCF sample of As adsorbed onto ferrihydrite (termed As(V)_Fh_coll (see section 5.3 for details), were collected at the European Synchrotron Radiation Facility (ESRF; 6 GeV, 100 mA) (bending-magnet BM25A Beamline) at room temperature. Ultrafiltration membranes with colloids were loaded into PEEK (polyether ether ketone) sample holders and sealed with Kapton tape. Depending on the As concentration, two or three membranes were loaded together to provide sufficient sample mass. Fluorescence spectra were collected using a 13-element Si-Li solid state detector and Si(111) monochromator crystals. The beam energy was calibrated for As on $KH_2AsO_4(s)$ by setting the maximum absorbance peak to 11875 eV. For Fe, energy was calibrated on metallic Fe foil by setting the first inflection of the absorption edge to 7112 eV.

6.2. Arsenic and iron XAS analysis

Arsenic and iron spectra were analyzed using Athena software [7] for linear combination fits, and EXAFSPAK software [8] for shell-by-shell fits. The background was subtracted using a linear fit through the pre-edge region. The spline fit through the extended X-ray absorption fine structure (EXAFS) region was performed using the Athena Autobak routine. Normalized As and Fe X-ray absorption near-edge structure (XANES) spectra were fit with linear least-squares combinations of reference compounds (see next section below). Initially for the XANES fits, 16 reference spectra were screened to determine a smaller set of

combinations of reference spectra that best matched the data. Consequently, a set of reference spectra consisting of scorodite ($FeAsO_4 \cdot 2H_2O$) and As adsorbed onto ferrihydrite for As XANES, and scorodite, phyllosilicates and Fe(III) oxide minerals for Fe XANES, were selected. Unknown spectra were then fit with all combinations of two or three reference spectra and ranked by statistical best fit (energy fixed). Finally, tests were performed with the highest ranking mixture of components to assess the sensitivity of the fit to the number of reference components, treating energy as a variable factor, and changing the spectral fit range. Fits were constrained to be non-negative, but not forced to sum to 100%. The relative goodness-of-fit between data and model is described by the reduced χ^2 value [=(F factor)/(#of points-#of variables].

Based on the results of the Fe XANES analysis, which indicated multiple components, linear combination fits (LCF) were performed on the Fe EXAFS spectra using the same set of reference spectra as for XANES fits. In contrast, As EXAFS data were analyzed using the shell-by-shell method (k-range $=2.0$ to $10\text{-}12.5$ Å^{-1} depending on data quality) with theoretical reference functions calculated using FEFF 8.0 software [9] based on atomic clusters from crystalline reference compounds calculated using ATOMS software [10]. Multiple scattering paths among bonded As and first-shell O atoms, resulting from the high symmetry of the arsenate tetrahedron, were included in the fit model in addition to single-scattering paths [11]. Interatomic distance (R), and either N (number of backscattering atoms) or $\square^2$ (Debye-Waller factor) were treated as variable factors for each atomic shell. Threshold energy (E_0) was treated as a single variable for all shells, and the scale factor (S_0^2) fixed at 1. The estimated errors based on empirical fits to reference compounds were: first shell: $R \pm 0.01$ Å, $\sigma^2 \pm 10\%$ (N fixed); other shells: $R \pm 0.02$ Å, $N \pm 25\%$ (σ^2 fixed) [11, 12].

6.3. As and Fe reference compounds

A natural scorodite reference compound (unspecified location, sample 65305) was obtained from the Stanford University Mineral Research Collection with an average composition of $Fe_{0.862} Al_{0.048} As_{0.93} P_{0.064} S_{0.006} O_4 d_n H_2O$ [13]. Arsenic and iron K-edge X-ray absorption spectra of scorodite were collected in transmission mode at the Stanford Synchrotron Radiation Laboratory beam line 4-3. Details of data collection are described in [13]. The reference (As(V)_Fh_coll) was prepared by equilibrating a 500 mg L^{-1} As(V) solution (ratio 1:100, solid:solution) with hydrous ferric oxide precipitated as two-line ferrihydrite [14] for 2 hours. The suspension was centrifuged at 800 rpm for 11 min to isolate the fraction <1000 nm. The colloid suspensions were ultrafiltered using 10 nm ultrafiltration membranes that

were loaded onto PEEK (polyether ether ketone) sample holders and sealed with Kapton tape. Arsenic and Fe XAS spectra were collected as described in Methods.

Arsenic and Fe K-edge EXAFS reference spectra were analyzed with the package EXAFSPAK [8] for shell-by-shell fits following the same procedure described in the manuscript for colloid samples, but now fixing the number of backscatterers (N) on crystallographic values and varying distance (R) and Debye-Waller factor (σ^2) for each atomic shell.

References

[1] G.W. Thomas, Exchangeable cations, in: A.L. Page (Ed.) Methods of Soil Analysis, Part 2. Chemical and Microbiological Properties, Soil Science Society of America, Madison, Wisc., USA. Illus, 1982, pp. P159-166.

[2] R. Barnhisel, P.M. Bertsch, Aluminum, Page, A. L. (Ed.). Agronomy: A Series of Monographs, Vol. 9. Methods of Soil Analysis, Part 2. Chemical and Microbiological Properties, 2nd Edition. Xxiv+1159p. American Society of Agronomy, Inc. Soil Science Society of America, Inc. Publishers: Madison, Wisc., USA. Illus, (1982) P275-300.

[3] L.M. Shuman, Comparison of exchangeable Al, extractable Al, and Al in soil fractions, Canadian Journal of Soil Science, 70 (1990) 263-275.

[4] A. Walkley, A.I. Black, An examination of the Degtjareff method for determining soil organic matter, and a proposed modification of the chromic acid titration method, Soil Science, 37 (1934) 29-38.

[5] S. Assemi, G. Newcombe, C. Hepplewhite, R. Beckett, Characterization of natural organic matter fractions separated by ultrafiltration using flow field-flow fractionation, Water Research, 38 (2004) 1467-1476.

[6] M.E. Schimpf, K. Caldwell, J.C. Giddings, Field-Flow Fractionation Handbook, Wiley & Sons, 2000.

[7] B. Ravel, ATHENA User's Guide 1.5, (2009).

[8] G.N. George, I.J. Pickering, EXAFSPAK: A suite of computer programs for analysis of X-ray absorption spectra, in, Stanford Syncrotron Radiation Laboratory, 2000.

[9] A.L. Ankudinov, B. Ravel, J.J. Rehr, S.D. Conradson, Real Space Multiple Scattering Calculation and Interpretation of X-ray absorption near-edge structure, Physical Review B, 58 (1998) 7565-7576.

[10] B. Ravel, ATOMS: crystallography for the X-ray absorption spectroscopist, Journal of Synchrotron Radiation, 8 (2001) 314-316.

[11] R.A. Root, D. Vlassopoulos, N.A. Rivera, M.T. Rafferty, C. Andrews, P.A. O'Day, Speciation and natural attenuation of arsenic and iron in a tidally influenced shallow aquifer, Geochimica et Cosmochimica Acta, 73 (2009) 5528-5553.

[12] P.A. O'Day, N. Rivera, Jr., R. Root, S.A. Carroll, X-ray absorption spectroscopic study of Fe reference compounds for the analysis of natural sediments, American Mineralogist, 89 (2004) 572-585.

[13] K.S. Savage, D.K. Bird, P.A. O'Day, Arsenic speciation in synthetic jarosite, Chemical Geology, 215 (2005) 473-498.

[14] U. Schwertmann, R.M. Cornell, Iron Oxides in the Laboratory, VCH Verlagsgesellschaft mbH, Weinheim, (Germany)

VCH Publishers, Inc., New York, (USA), Weinheim, Germany, 1991.